ARTICLE OPEN

Check for updates

Corrosion-induced hydrogen evolution, absorption, and cracking behaviors of ultra-high-strength galvanized and galvannealed steel sheets

Sung Jin Kim[1]✉, Jin Sung Park[1] and Seung-Pill Jung[2]

Various experimental analyses on hydrogen evolution, absorption, and cracking behaviors were conducted to gain a fundamental understanding of the hydrogen embrittlement of ultrastrong steel sheets with galvanized (GI) and galvannealed (GA) coatings. The hydrogen evolution and absorption behaviors are controlled primarily by the potential differences between the coating and exposed steel substrate, and the corrosion-induced damage pattern of the coating. The higher absorption rate of hydrogen was more pronounced in corroded GI-coated steel caused by the larger cathodic polarization applied to the exposed substrate, and a more severe form of coating dissolution by aqueous corrosion in a 3.5% NaCl + 0.3% NH_4SN solution. In contrast, the corrosive species can only penetrate through the pre-existing cracks in the brittle Fe-Zn intermetallic phases composed of the GA coating, and the driving force for hydrogen evolution becomes smaller. These result in significant differences in hydrogen penetration and cracking behaviors between the two coated ultrastrong steels.

npj Materials Degradation (2022)6:31 ; https://doi.org/10.1038/s41529-022-00245-1

INTRODUCTION

With the growing environmental awareness and stricter regulations on emissions, the automotive industry is facing significant challenges. Among them, the application of lightweight materials centered on ultra-high-strength steel sheets is considered one of the major technical issues[1–4]. Ultra-high-strength steel sheets with a tensile strength of >1500 MPa have been developed and employed in some auto-parts. On the other hand, the higher strength of the steel sheet raises significantly a concern regarding hydrogen embrittlement and pre-mature cracking failures[1,4–7]. When steel is exposed to atmospheric/aqueous environments during the service, hydrogen atoms can be generated by cathodic reduction[8–10] or hydrolysis reactions[10,11] on the surface. Some of them are infused into the steel matrix and are trapped at metallurgical defects, leading to hydrogen embrittlement[12,13].

Some auto-parts are coated with Zn-based alloys to provide an anti-corrosion function, and they have been employed under the name of galvanized steels with a hot-dip Zn coating (GI). For additional improvements in weldability and paintability, a galvannealed (GA) coating, composed of several distinctive Zn–Fe intermetallic layers, is also used by annealing the GI coating at 500~600 °C[14–16]. The primary function of both coatings is based on galvanic protection of the underlying steel substrates from corrosion because the coatings have much lower electrochemical potentials under most corrosive conditions[17,18]. On the other hand, the sacrificial dissolution characteristics of Zn and Zn–Fe coatings, providing an effective anti-corrosion function, can be the primary driving force for hydrogen evolution on a steel surface. Theoretically, the exchange current density for hydrogen evolution reaction on Zn, and the diffusion coefficient of hydrogen in Zn with a hexagonal close-packed (HCP) structure are much lower than the case of Fe[7,19–21], and the danger of hydrogen infusion would not be expected. Once the coatings are damaged locally, however, a galvanic couple between the coatings and steel substrate can be formed, and the applied large cathodic polarization on the exposed steel substrate can promote hydrogen evolution. Nevertheless, the hydrogen evolution and absorption mechanism under a neutral aqueous corrosion system are unclear. Furthermore, the extent and kinetics of the coating damage caused by the corrosion reaction can depend significantly on the composition and structure of the coatings. These suggest that the corrosion damage and even the hydrogen evolution and penetration behaviors can be different in GI and GA coatings.

Therefore, this study examined the hydrogen evolution, absorption, and hydrogen-induced cracking behaviors of the GI and GA-coated steel sheets during the surface degradation of coatings in a neutral aqueous environment, using a combination of electrochemical polarization, electrochemical permeation, and metallographic observation of coating dissolution. For a further mechanistic approach, the polarization behaviors were analyzed by a numerical model based on the mixed potential theory. Moreover, the hydrogen absorption in the charging side of the permeation cell was interpreted by galvanic current flow from the coating layer to the bare steel using a modified permeation apparatus.

RESULTS

Samples and their microstructures

The materials under investigation were GI and GA-coated ultra-high-strength steel sheets with a tensile strength of >1500 MPa. The chemical composition of the steel substrate, and variables of the GI and GA processes are listed in Tables 1 and 2, respectively.

Figure 1 presents the microstructure of the cold-rolled and normalized (CR_N) steel sample without the coating. The

[1]Department of Advanced Materials and Metallurgical Engineering, Sunchon National University, Jungang-ro, Suncheon, Jeonnam 540-742, Republic of Korea. [2]Automotive Steel Application Engineering Team, Technical Research Center, Hyundai-Steel, 1480, Buckbusaneop-ro, Songak-Eup, Dangjin-Si, Chungnam 343-823, Republic of Korea.
✉email: sjkim56@scnu.ac.kr

microstructure consisted of the lath-type tempered martensite with randomly oriented ferrite and fine Fe_3C in small quantities (4.1%). The fine precipitates below 100 nm distributed uniformly throughout the matrix were shown in Fig. 2. The precipitates were classified into two types according to their size. Fe_3C and TiN are precipitates, 50–100 nm in size (Fig. 2b), and (Ti-Mo)C,N <20 nm in size (Fig. 2c).

Table 1. Chemical composition of the ultra-high-strength steel substrate.

Chemical composition (wt.%)									
Fe	C	Si	Mn	P	S	Cr	Ni	Cu	Mo
Bal.	0.28	0.09	1.85	<0.01	<0.01	0.36	0.012	0.021	0.19

Table 2. Variables for the GI and GA coating processes.

GI and GA coating processes		
Coating samples	GI	GA
Steel thickness	1.2 mm	
Zn bath temperature	450–470 °C	
Galvannealing temperature	–	520–580 °C
Coating thickness	10–12 μm	7–8 μm

Figure 3 shows FE-SEM images of the surface and cross-section morphologies of GI and GA-coated steels. In contrast to the GI coating with only a η-Zn single-phase, ~10 μm thick, the GA coating was much thinner (<7 μm thick), and composed of multi-layers with different phases. According to the diffraction pattern by TEM (Fig. 3g) and compositional analysis by EDS (Table 3), the layer was composed of several Zn–Fe intermetallic Γ, δ, and ζ phases in the order from the steel substrate. Previous studies[22–24] reported also that the Fe contents of the outermost ζ phase, middle δ phase, and bottom Γ phase were ~6–7, 10–12, and >23 wt.%, respectively, which correspond to the those analyzed in this work. The other differences between the two coatings are the types of defect in the coating layers. The (Al,Fe)-based fine particles known as a top-dross (Fig. 3d), and the vertical cracks from mostly δ phase to steel substrate (Fig. 3h) are the characteristic defects in the GI and GA coating layers, respectively.

Electrochemical potentiodynamic polarization behaviors

Figure 4a presents the electrochemical potentiodynamic polarization curves of CR_N steel (i.e., bare steel), and GI and GA-coated steel samples, obtained in a 3.5% NaCl + 0.3% NH_4SCN solution. As expected, GI and GA-coated steel samples had much lower corrosion potential than CR_N steel. Although the polarization behaviors between the two coating layers show a similar trend, the corrosion potential of the GA coating layer composed of Zn–Fe intermetallic phases was slightly higher than that of the GI coating layer consisting of only pure Zn. When the GA coating is corroded, the order of exposure to the corrosive environments would be the outermost ζ, middle δ, and bottom Γ phase.

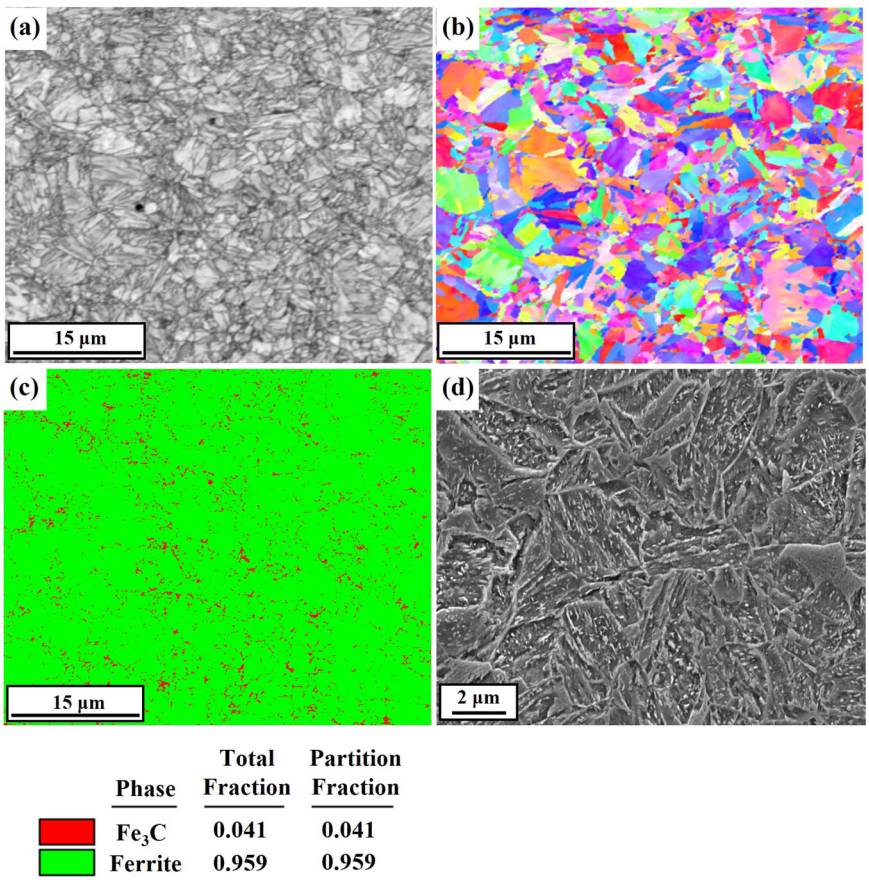

Fig. 1 Microstructural analysis of steel substrate. a–c EBSD image quality map, inverse pole figure map, and phase colored map, respectively. **d** FE-SEM observation.

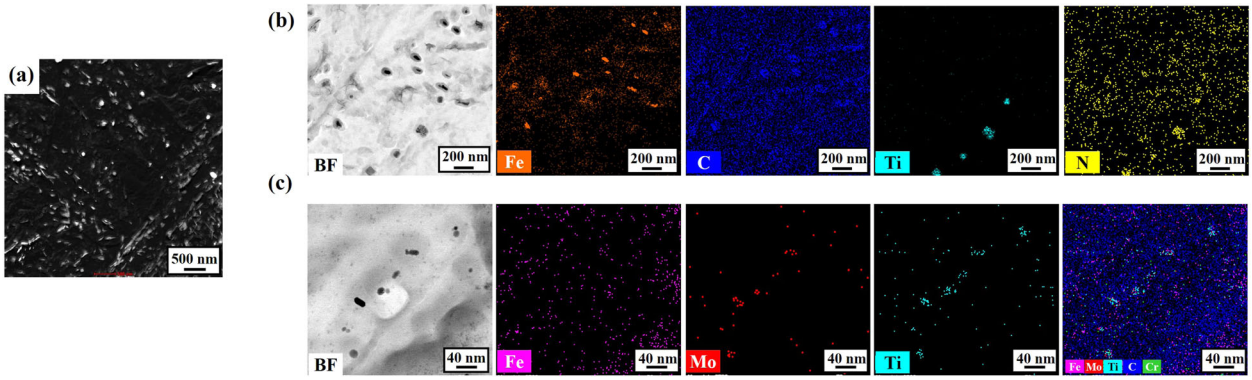

Fig. 2 Analysis of precipitates in steel substrate. a TEM-dark field image, which were obtained by the replica extraction method. **b, c** TEM observations (bright-field image) with EDS mapping of precipitates with the size in the range of 50–100 nm, and <20 nm, respectively.

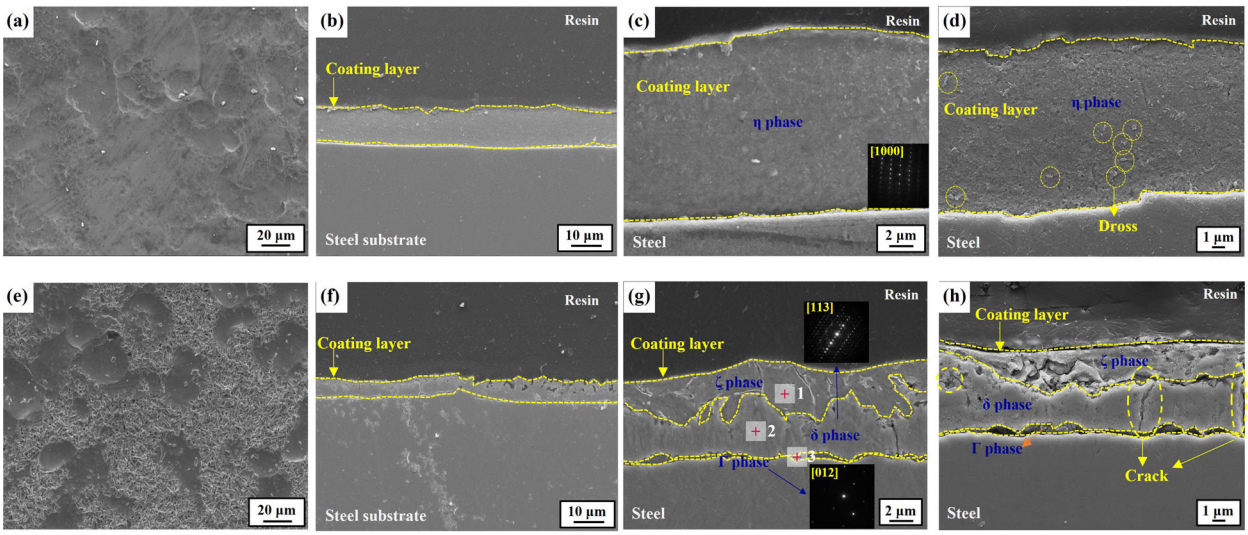

Fig. 3 FE-SEM images showing the microstructures of the coating layers. a, b Surface and cross-section morphologies of GI, respectively. **c, d** Magnified images of **b**. **e, f** Surface and cross-section morphologies of GA, respectively. **g, h** Magnified images of **f**.

Table 3. EDS quantitative analysis at each point marked on Fig. 3.

	Fe (wt.%)	Zn (wt.%)
ζ (+1)	7.0	93.0
δ (+2)	12.8	87.2
Γ (+3)	23.6	76.4

Considering that the electrochemical potentials of the phases increase in the order of ζ, δ, and Γ owing to their Fe contents, the corrosion potential becomes nobler as corrosion of the GA coating progresses. The corrosion behavior of multi-layered GA-coated steel, mentioned above, can also be validated through the electrochemical stripping test results, as shown in Figs. 5–7. The potential transition curve of GI-coated steel, obtained in a 3.4 M NaCl + 0.3 M $ZnSO_4$ solution, showed only two plateau potential regions, marked with red boxes and signs (a and b), corresponding to η-Zn phase and substrate, respectively. In contrast, several plateau points, marked with red boxes and signs (a, b, c, and d) in Fig. 5b, during the increase in potential by the dissolution of each phase composed of GA- coated steel. From the metallographic observations at points (a–d) in Fig. 5b, shown in Fig. 6, the plateaus a, b, c, and d were attributed to the exposure to ζ phase, δ phase, Γ phase, and substrate, respectively. It also showed that the corrosion potential, measured after the stripping test at respective potential steps (a, b, c, and d) marked on Fig. 5b became nobler (Fig. 7).

Electrochemical hydrogen permeation behaviors

The hydrogen permeation behaviors under applied cathodic current in the charging side are presented in Fig. 8a. Theoretically, a constant amount of hydrogen can be introduced by excluding any corrosion and scale forming processes. The current densities measured in the detection side (i.e., permeation flux) of GI and GA-coated samples were significantly smaller and the break-through time to diffuse was considerably longer compared to the case of CR_N steel. Nevertheless, comparatively higher permeation flux and much shorter break-through time were obtained in the GA-coated steel.

In contrast to the permeation results given above, it is interesting to note that, in the absence of an externally applied current, only GI-coated steel exhibits abrupt increases in permeation current in significantly large quantities (Fig. 8b), suggesting that hydrogen evolution and absorption were enhanced much more on the steel substrate with the corroded GI coating. In a similar context, the galvanic current flow from the coatings to bare

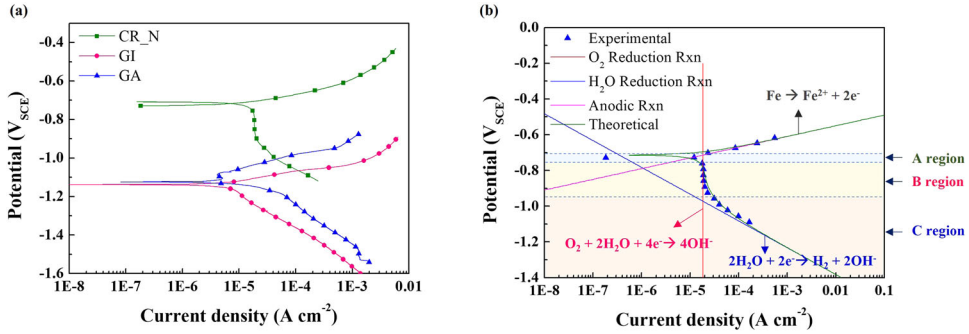

Fig. 4 Electrochemical corrosion behaviors. a Potentiodynamic polarization curves obtained in a 3.5% NaCl + 0.3% NH_4SCN solution. **b** Numerical curve-fitting to **a**.

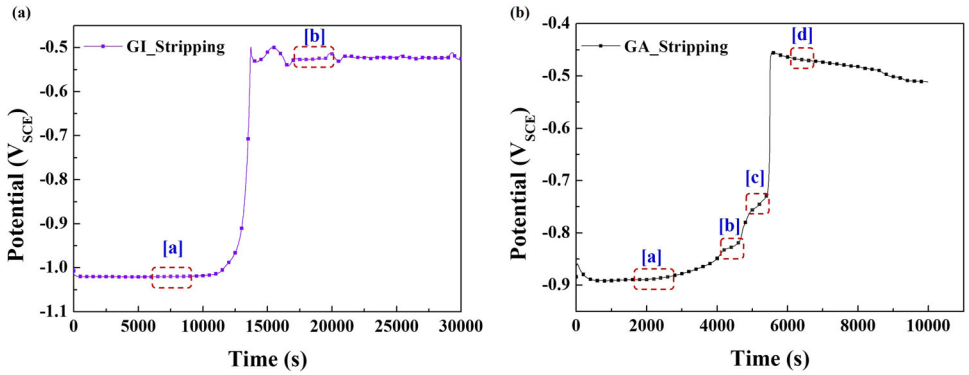

Fig. 5 Potential transition curves obtained from electrochemical stripping test in a 3.4 M NaCl + 0.3 M $ZnSO_4$ solution. a, **b** GI and GA, respectively.

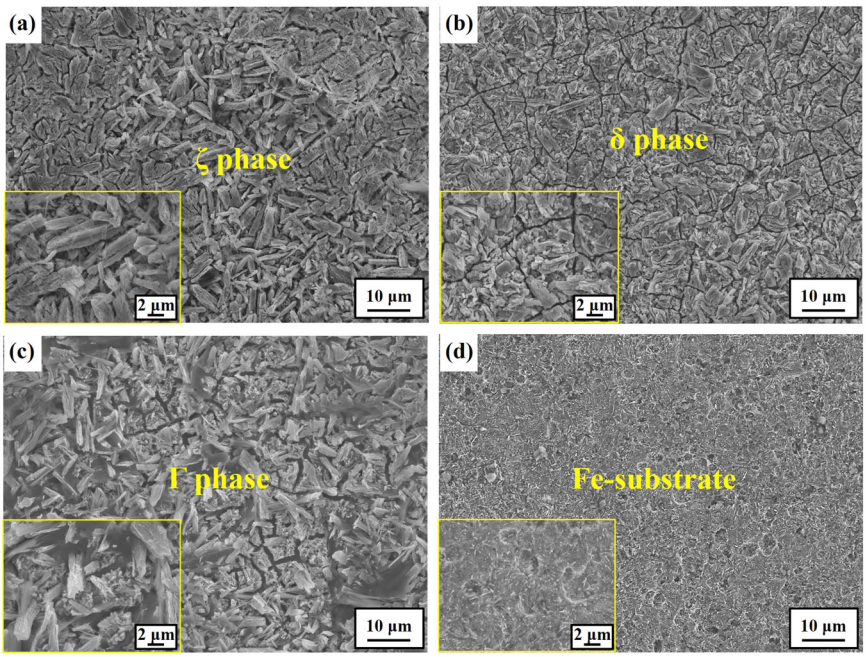

Fig. 6 Surface morphologies of GA sample during electrochemical stripping test in a 3.4 M NaCl + 0.3 M $ZnSO_4$ solution. a–d FE-SEM observations at respective potential steps marked on Fig. 5b.

steel, and permeation flux of hydrogen reduced cathodically on the bare steel surface, under the simple immersion corrosion condition (described schematically in Fig. 8c), were much higher in the case of GI coating, as shown in Fig. 8d.

Corrosion with coating dissolution behaviors

To clarify the permeation behaviors in an absence of cathodic polarization condition, a more precise understanding of the corrosion progresses involving the dissolution behaviors of the

sacrificial coating is required. The changes in the cross-section morphologies of the two coated steel samples with increasing immersion in a neutral aqueous environment (i.e., 3.5% NaCl + 0.3% NH_4SCN solution) suggest clear differences in coating damage between the two coating layers, as shown in Fig. 9. At the early stages of immersion for 24 h, the outermost ζ phase in the GA coating layer dissolved rapidly. It appears also that the pre-existing cracks and pores, which are found mostly in the δ phase, may serve as a penetration path for corrosive species, even into the steel substrate. The reactive areas may increase gradually due to the broadening of the existing cracks and the development of new cracks.

On the other hand, there was no preferential dissolution at certain areas in the GI coating layer at the early stages of immersion. On the outer part of the GI coating layer, some localized crack-like attacks appear gradually with increasing immersion time to 24 h. As assumed from the magnified inset figure, the grain boundary of the coating layer is the main propagation path of the crack-like corrosion attack. Subsequently, the dissolution rate of the coating layer may be so severe that the area of the substrate without a coating layer, which can be exposed to the outer environment, becomes comparatively larger. It seems that some parts of the coating were detached from the steel substrate with continued corrosion attacks along the grain boundary. These morphological differences between the two coating layers can also be demonstrated by surface analysis of the corroded coating layers employing a three-dimensional surface profiler, as shown in Fig. 10. Owing to the local detachment of the coating layer, the value of R_a, measured in the GA-coated steel sample, was much higher than that in GI-coated steel.

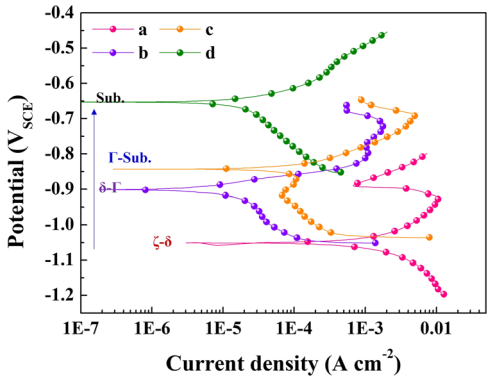

Fig. 7 Potentiodynamic polarization curves of the GA-coated steel in a 3.5% NaCl + 0.3% NH_4SCN Solution. Measured after electrochemical stripping test in a 3.4 M NaCl + 0.3 M $ZnSO_4$ solution at respective potential steps marked on Fig. 5b.

Cracking susceptibility

The resistance to hydrogen-assisted cracking failures caused by aqueous corrosion between the two coated steel samples was compared by a four-point bent beam test conducted in a neutral aqueous environment (i.e., 3.5% NaCl + 0.3% NH_4SCN solution).

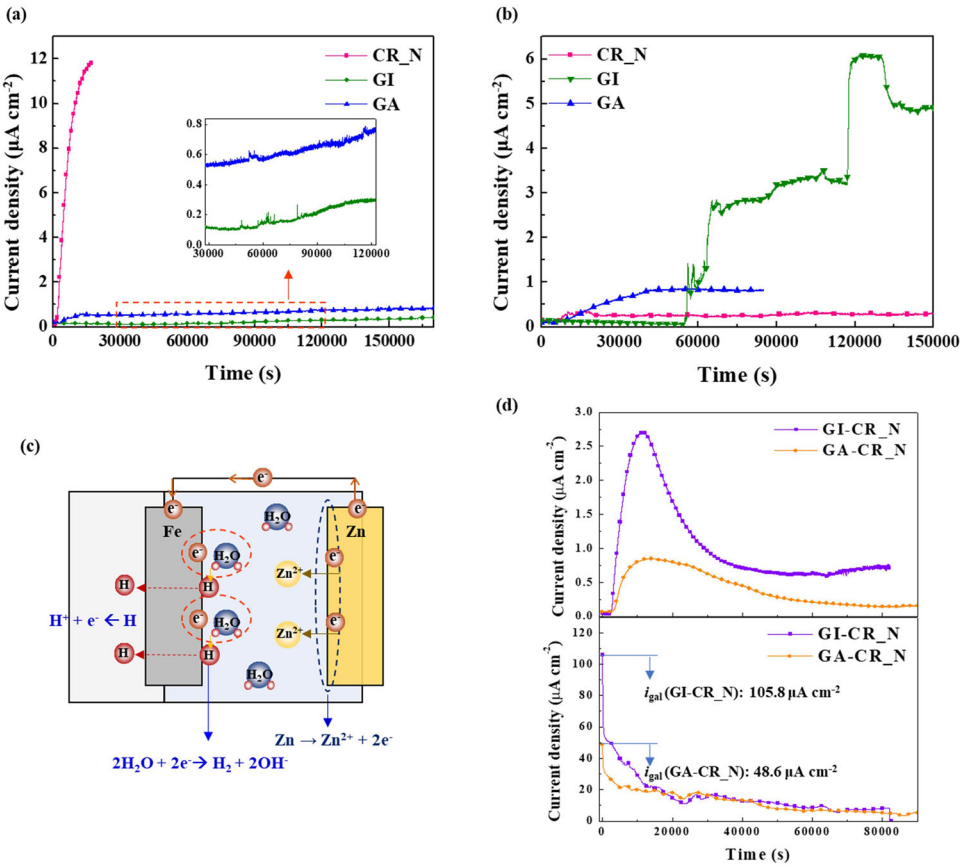

Fig. 8 Electrochemical and simple corrosion induced hydrogen permeation behaviors. a, **b** Electrochemical permeation curves obtained using the typical permeation apparatus with and without the application of cathodic current in the charging side, respectively. **c** Brief sketch showing the principle of the hydrogen permeation measurements using the modified permeation apparatus with the galvanic corrosion cell in the charging side. **d** Hydrogen permeation current densities and galvanic current densities measured in detection side and galvanic corrosion side, respectively, of the modified permeation apparatus.

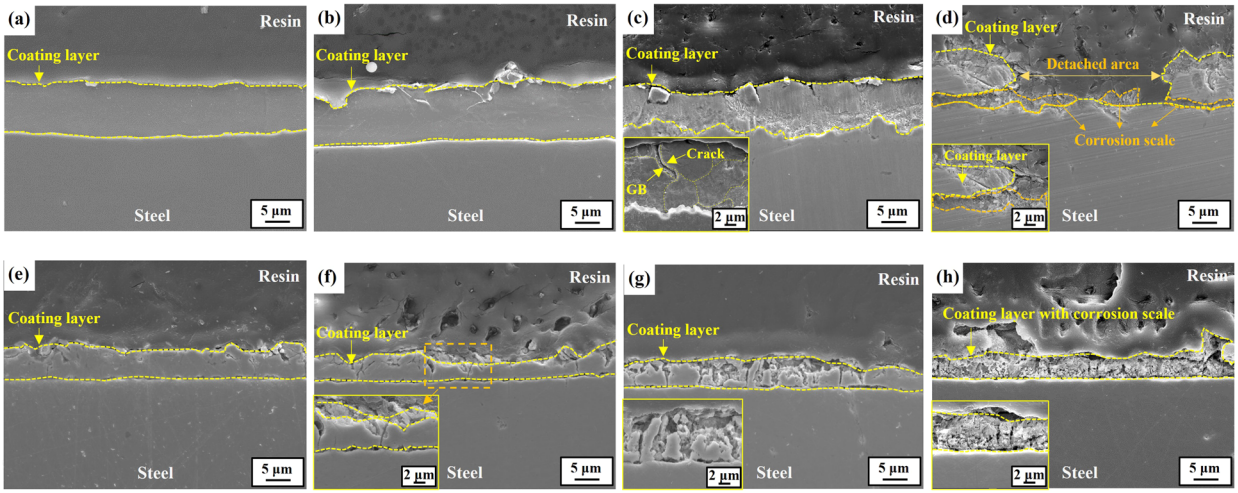

Fig. 9 Change in the cross-section morphologies with increasing immersion times. a–d GI-coated steel. **e–h** GA-coated steel. **a**, **e** three h. **b**, **f** 24 h. **c, g** 72 h. **d, h** 168 h.

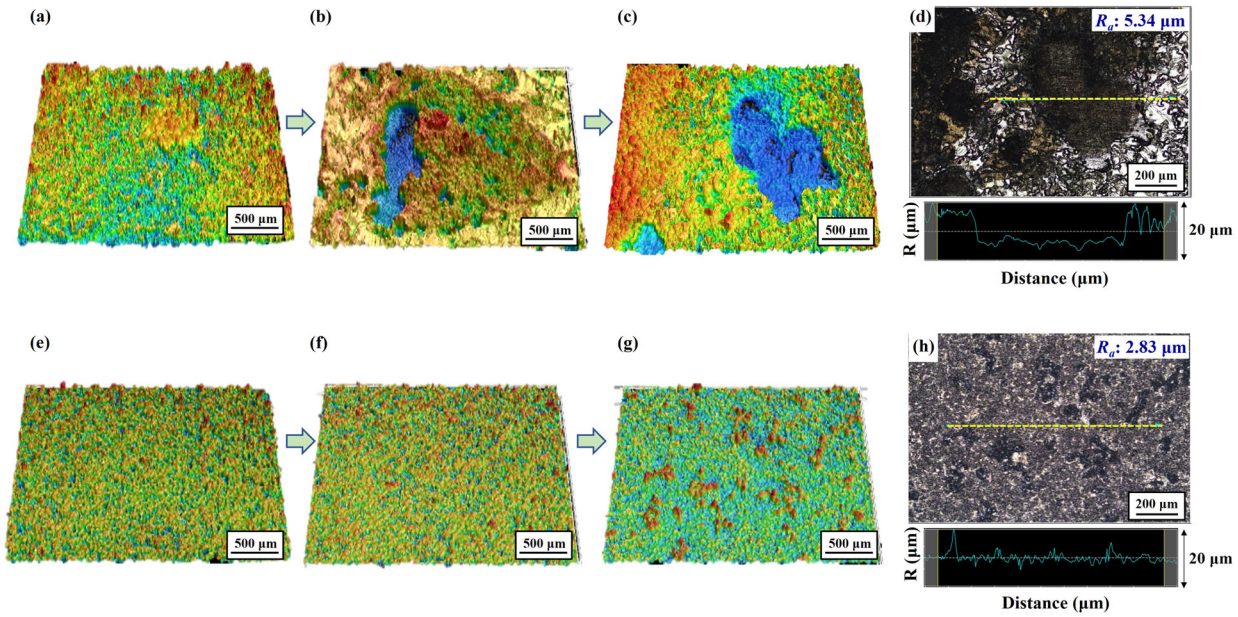

Fig. 10 Three-dimensional surface roughness measurements with increasing immersion times. a–d GI-coated steel. **e–h** GA-coated steel. **a**, **e** 24 h. **b**, **f** 72 h. **c**, **d, g, h** 168 h.

As shown in Fig. 11, in contrast to GA-coated steel samples, GI-coated steel samples failed within a day of immersion. Unlike the typical dimple fracture obtained normally in the open air, quasi-cleavage with an intergranular fracture pattern was observed in the fracture surface of the GI-coated steel sample, as shown in Fig. 11c, d.

DISCUSSION

The higher strength of >1500 MPa of the steel substrate could be attributed mainly to the effective strengthening via fine precipitates below 100 nm distributed uniformly throughout the matrix. In particular, among the two types precipitates, finer precipitates, (Ti-Mo)C,N, characterized in this work, are generally considered more effective in impeding the movement of dislocations[25,26], which can be the primary strengthening mechanism of ultra-high-strength steels. The effects of the partial substitution of Mo for Ti in the TiC lattice on the nucleation and coarsening kinetics of MC carbide and the strengthening of steel are also reported elsewhere[27].

Regarding the electrochemical corrosion behaviors, the anodic regions of the curves involve generally metal dissolution (i.e., $M \rightarrow M^{n+} + ne^-$, where M can be steel or Zn-based coating) on the electrode surface. Hence, the anodic reaction is controlled by a charge transfer process, which can be simulated by pure Tafel behavior, as described in Eq. (1).

$$E - E_0 = \beta_a \log\left(\frac{i}{i_0}\right) \quad (1)$$

where E, E_0, β_a, i, and i_0 are the electrode potential in V_{SCE}, standard electrode potential in V_{SCE}, anodic Tafel slope in V decade^{-1}, current density in A cm^{-2}, and exchange current density in A cm^{-2}, respectively.

In contrast, there could be two possible cathodic reactions involved in the neutral aqueous system, depending on the potential regions. One is the reduction of oxygen ($O_2 + 2H_2O + 4e^- \rightarrow 4OH^-$),

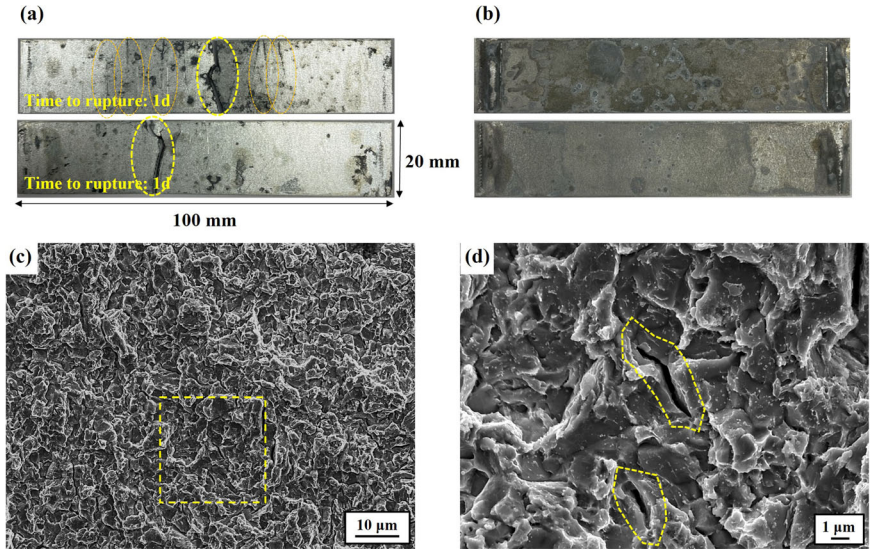

Fig. 11 Surface view of test samples after four-point bent beam test, and fracture surface observations. a, b GI and GA-coated steel samples, respectively. **c** FE-SEM image showing the fracture surface of the GI-coated steel. **d** Magnification of the boxed region marked on **c**.

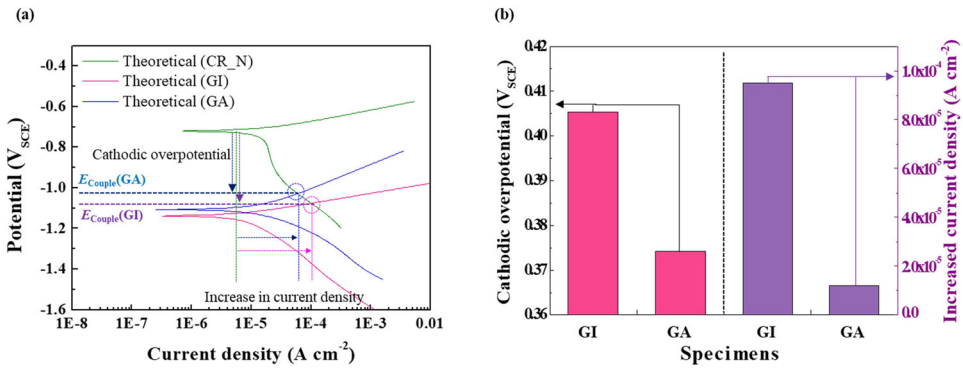

Fig. 12 Electrochemical analysis of galvanic couple (steel substrate-two types of coated steel). a Potentiodynamic polarization curves obtained in a 3.5% NaCl + 0.3% NH_4SCN solution, indicating the galvanic couple potentials (E_{couple} (GI-CR_N), E_{couple} (GA-CR_N)), applied cathodic polarization levels on CR_N with GI and GA, respectively, and the increased current densities on CR_N, polarized cathodically, by galvanic coupling with GI and GA, respectively. **b** Quantitative representation of the parameters (applied cathodic polarization and increased current density), marked on **a**.

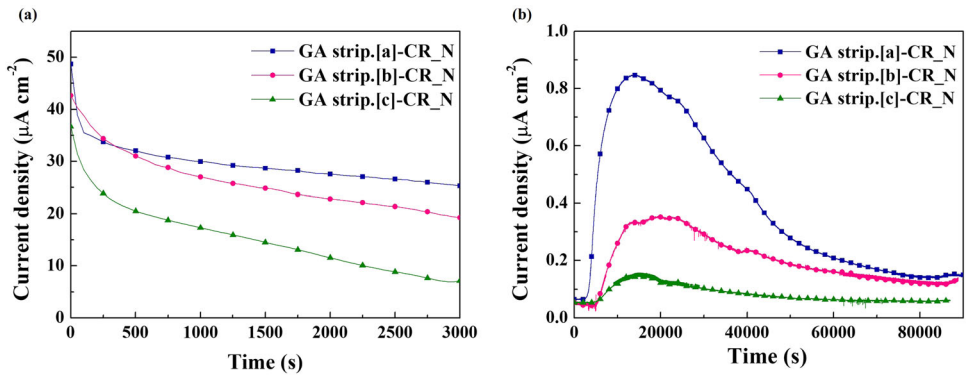

Fig. 13 Galvanic corrosion and hydrogen permeation behaviors using the modified permeation apparatus. a Galvanic corrosion current densities between the bare steel and stripped GA samples, obtained at respective potential steps (marked as **a**–**c** on Fig. 5b) in an electrochemical stripping test in a 3.4 M NaCl + 0.3 M $ZnSO_4$ solution. **b** Hydrogen permeation current densities measured in the detection side of bare steel as a result of **a**.

Table 4. Various corrosion parameter values obtained by numerical curve-fitting to potentiodynamic polarization data of the tested samples.

	$i_{0\_H_2O}$ (A cm^{-2})	$\beta_{a\_steel/coating}$ (V dec^{-1})	$\beta_{c\_H_2O}$ (V dec^{-1})	$i_{lin\_O_2}$ (A cm^{-2})	i_{corr} (A cm^{-2})	E_{corr} (V_{SCE})
CR_N	1.0×10^{-7}	0.06	0.15	1.85×10^{-5}	2.13×10^{-5}	−0.710
GI	8.8×10^{-8}	0.05	0.22	1.00×10^{-5}	1.29×10^{-5}	−1.116
GA	9.5×10^{-8}	0.15	0.20	1.20×10^{-5}	1.82×10^{-5}	−1.084

which is controlled by mixed charge transfer and mass transfer. The other is the reduction of water molecules ($2H_2O + 2e^- \rightarrow H_2 + 2OH^-$), controlled only by charge transfer due to the unlimited number of water molecules on the electrode interface. Hence, the net current density for O_2 reduction can be derived theoretically using Eq. (2)[28].

$$\frac{1}{i_{O_2}} = \frac{1}{i_{c\_t}} + \frac{1}{i_{m\_t}} \quad (2)$$

where i_{O_2}, i_{c_t}, and i_{m_t} are the net O_2 reduction current density, charge transfer current density, and mass transfer current density, respectively.

The charge transfer current density can be obtained from the conventional Tafel behavior, as described in Eq. (1). On the other hand, the concentration of O_2 in the bulk solution, diffusion coefficient of O_2, and thickness of the diffusion boundary layer can also be considered for the mass transfer current density. These parameters, adopted in our numerical analysis, were obtained from the previous work by L. Chen et al.[28].

As noted above, the reduction of H_2O can only be controlled by charge transfer, and was interpreted from the conventional Tafel behavior described in Eq. (1).

Consequently, the corrosion potential and corrosion current density were determined by the charge balance theory, as described below.

$$i_{corr} = i_{Fe} = i_{O_2} + i_{H_2O} \quad (3)$$

where i_{Fe}, i_{O_2}, and i_{H_2O} are the anodic steel dissolution current density, O_2 reduction current density, and H_2O reduction current density, respectively.

From the numerical curve-fitting to the polarization data, which was conducted based on mixed potential theory and charge balance equation, the results for CR_N are presented in Fig. 4b as a representative. The fitted parameters for CR_N and two coatings are listed in Table 4. Overall, the theoretical curve based on the numerical model showed good agreement with the experimental curve. The cathodic curve could be classified into three regions (A, B, and C) with a negative shift of potential. In the A region, the reduction of dissolved O_2 at the electrode/solution interface, which is controlled by charge transfer, would be the dominant reaction. From the limiting current features (i.e., diffusion-limited current) in the B region, the reduction of dissolved O_2 is controlled primarily by O_2 diffusion. With further decreases in potential (C region), the reduction of H_2O becomes the dominant reaction, and hydrogen can be evolved on the electrode surface.

Although the polarization behaviors between the two coating layers show a similar trend, the dissolution of multi-layered GA coating can lead to the increase in corrosion potential gradually as corrosion progresses, which is in contrast to the GI coating with only a η-Zn single-phase. This can have significant meaning in that the driving force for hydrogen evolution would be lowered. Theoretically, it is considered that the amount of hydrogen permeated through the Zn/Zn alloyed coatings without defects can be negligible because of the slow kinetics of hydrogen generation on the coating surface[19,21,29] and the significantly low diffusion coefficient of hydrogen atoms in the coating layer[19,20,30]. This theoretical approach, however, has no practical meaning, and the danger of hydrogen-assisted failures could increase substantially when the coating layer has pre-existing defects or pores. In particular, when the galvanic couple between the coating layer and steel substrate is formed by local damage/dissolution of the coating layer during corrosion, the exposed steel substrate can be forced to be polarized cathodically to a less noble potential near the corrosion potential of the phase in the coating layer. This suggests that the exposed substrate can serve as cathodic sites where hydrogen is generated by the reduction of H_2O. As higher cathodic polarization is applied to the steel substrate, more hydrogen can be generated by the reduction of H_2O (Fig. 4b). These also suggest that the driving force for hydrogen generation on the exposed steel substrate near the damaged GI coating layer could be higher compared to the case of GA-coated steel. Hence, under an assumption that the surface area ratios between the coatings and their substrates are the same, the galvanic couple between GA coating and substrate can have the smaller cathodic polarization applied to the substrate, as shown in Fig. 12a. When a further increase in corrosion potential of the GA coating with corrosion progresses, the dominant reduction reaction would be the reduction of dissolved O_2, not the reduction of H_2O. The increased cathodic currents under applied polarization cathodically to the steel substrate were determined, as shown in Fig. 12b. Nevertheless, the increased current density cannot be considered the amount of hydrogen absorbed directly because of the partial recombination of hydrogen ($H + H \rightarrow H_2$) on the surface. Therefore, the hydrogen permeation behaviors of the two coated steel samples under the corrosion process in the charging side should be analyzed further.

Under applied cathodic overpotential condition, the hydrogen permeation fluxes of the two coated steel samples were significantly lower than that of CR_N steel, owing to the much slower diffusion kinetics of atomic hydrogen in the Zn and Zn–Fe layers. The hydrogen diffusivity values in the GI and GA coating layers calculated by the following Eq. (4)[31] based on the 2nd permeation fluxes were 2.2760×10^{-14} m^2 s^{-1} and 1.6053×10^{-13} m^2 s^{-1}, respectively, which were much higher than the previously reported ones in Zn (~10^{-15} m^2 s^{-1})[31] and Zn–Fe intermetallic layer (4.0457×10^{-14} m^2 s^{-1})[30].

$$\frac{L_1}{D_1} + \frac{L_2}{D_2} = \frac{L_{1+2}}{D_{app}} \quad (4)$$

where L_1 and L_2 are the thicknesses of substrate and coating, respectively, and D_1, D_2, and D_{app} are the apparent hydrogen diffusivities in the substrate, coating, and coated substrate, respectively. D_1 and D_{app} were determined experimentally using the time-lag method.

Theoretically, the hydrogen permeation behaviors of metallic materials under applied cathodic polarization depend greatly on the crystal structure of materials and their metallurgical defects. Hence, the faster diffusion kinetics of hydrogen in the two coating layers compared to those reported previously may be due to the presence of metallurgical defects in the coating layers. In particular, comparatively higher permeation flux and shorter break-through time of GA-coated sample than those of GI-coated sample can be understood by the fact that the hydrogen atoms absorbed in GA-coated steel are preferentially penetrated through the pre-existing defects in the coating layer. In contrast to the GI coating layer, the multi-layered intermetallic phases in the GA coating layer are more brittle with Vickers hardness of >250 H_V[32]. Hence, the cracks can be more likely to occur in the GA

coating layer during the skin pass milling conducted after the galvanizing process. As shown in Fig. 3h, the δ phase in the GA coating layer has several pre-existing cracks. The surface of pre-existing cracks can act as a high diffusion path for atomic hydrogen, resulting in an increase in the hydrogen diffusion kinetics and higher permeation flux.

Under no applied cathodic polarization condition, however, only GI-coated steel exhibits the abrupt increase in permeation current density in large quantities (Fig. 8b). This suggests that hydrogen evolution and absorption were enhanced much more on the steel substrate with the corroded GI coating. Compared to a previous study[33] that reported the level of hydrogen uptake at the cut-edges or scratches in GI-coated steel, the permeation current density presented in this study appeared to be higher. The cause of this difference can be considered with respect to the following two factors. The smaller surface area of the exposed steel in an advanced state of corrosion, as in this study, can provide less alkaline conditions, resulting in higher hydrogen activity. The other is that using a recombination inhibitor (i.e., NH_4SCN) in this study can further increase the hydrogen absorption in GI-coated steel. In the absence of a recombination inhibitor, the permeation current density of GI was much lower, as shown in Supplementary Fig. 1. Nevertheless, the overall trend of permeation current density was similar. Both cases showed an abrupt increase in current density after the long incubation times in the advanced state of corrosion. On the other hand, the permeation current density of GA in the advanced state of corrosion in the absence of a recombination inhibitor was not measured in the preliminary test, which may be ascribed to the extremely low current level that is difficult to measure using the permeation technique with the Devanathan-Stachurski (DS) cell. In contrast to the GI coating, much faster diffusion kinetics of hydrogen in smaller quantities was obtained in GA-coated steel in the presence of NH_4SCN (Fig. 8b). Under the corrosion condition, hydrogen penetration behaviors are controlled primarily by the corrosion-induced damage pattern of the coating layer. In the case of GA-coated steel, δ and Γ intermetallic phases and the steel substrate are connected electrically, they corrode together. Specifically, the Γ phase can dissolve prior to the δ phase due to the larger potential difference between the Γ phase and the substrate, as reported previously[23]. Therefore, it is expected that the driving force for hydrogen evolution by the H_2O reduction on GA-coated steel becomes smaller as corrosion proceeds (i.e., smaller cathodic overpotential applied by the galvanic couple between the Γ phase and steel substrate). This can also be further validated by the experimental result (Fig. 13) that the galvanic current flow from each phase in GA coating, obtained by stripping method, to bare steel, and the permeation flux of hydrogen reduced cathodically on the bare steel was decreased in the order of ζ, δ, and Γ, which is in accordance with the order of the potential difference. The much smaller permeation flux maintained in the GA-coated steel samples, as presented in Fig. 8b and d, can be understood in this regard. On the other hand, both electrochemical analysis and metallographical observation indicated that much faster dissolution rate of the GI coating layer and local detachment of the coating layer by aqueous corrosion leaves a broader area of the exposed substrate in GI-coated steel. Moreover, the comparatively larger cathodic polarization can be applied to the exposed substrate near the Zn layer (i.e., a higher hydrogen evolution by H_2O reduction), as evidenced by the higher galvanic current flow from the GI coating to bare steel (Fig. 8d). These result in the abrupt increase in permeation current density in large quantities of GI-coated steel sample. Regarding the rapid decrease in permeation current densities, shown in Fig. 8d, there are several possible explanations. The quick initial decrease after reaching the maximum current density is most likely due to an increase in pH on the steel surface via the reduction reactions and to the inhibitive effect by the Zn cations[34,35]. The gradual decrease in current density after longer times in permeation could be resulted from both the decrease in the Zn coating present on the sacrificial anode used polarizes the steel, and the formation of corrosion products on the corroding Zn coating. Based on the results and discussion given above, the mechanistic differences in the corrosion damages and resulting hydrogen penetration behaviors between the two coated steel samples are illustrated schematically in Fig. 14.

Compared to the corrosion behaviors of GA-coated steel, the preferential corrosion attacks along the grain boundary and much broader corrosion damage in the GI coating layer can lead to a much larger quantity of hydrogen absorbed and permeated in the steel substrate, resulting in higher susceptibility to the hydrogen-assisted cracking failures. The higher susceptibility to the intergranular cracking of GI-coated steel was evidenced experimentally by a four-point bent beam test conducted in a neutral aqueous environment. The hydrogen contents in as-galvanized samples, measured by thermal desorption method, were quite small (<5 ppb), and the difference between the two coated steels was insignificant. In addition, the steel substrate without the Zn-based coatings did not fail in the bent beam test. These suggest that the steel matrix can be embrittled and failed primarily by abundant atomic hydrogen, which had been absorbed on the exposed steel substrate during corrosion of the coating layer. Moreover, the locally concentrated hydrogen at corrosion-induced damaged areas (i.e., GI case) can be more critical to this hydrogen-induced cracking failure than the globally dispersed ones at numerous pre-existing cracks in the coating layer (i.e., GA case). Compared to simple immersion, the bent beam could provide more severe conditions in terms of corrosion damage in the coating layer and hydrogen absorption in the steel substrate[36–38], which may facilitate cracking failure. Nevertheless, the GA-coated steel samples did not fail after five days of immersion. This suggests that applying the GA coating to ultra-high-strength steels can be considered more positively in terms of hydrogen-assisted failures occurring in an advanced state of corrosion, though the GI coating is known to provide better sacrificial protection, particularly at cut-edges or scratches.

In summary, this work provided significant insights into the hydrogen evolution, absorption, and cracking behaviors of GI and GA coatings on ultra-high-strength steel surfaces during the surface degradation of the coatings in a neutral aqueous environment. When the coating layer was undamaged, the amount of hydrogen absorbed on the surface and permeated through the coating and substrate was negligible because of the much slower kinetics of hydrogen diffusion in the coating layer. On the other hand, the amount increased significantly when the steel substrate was exposed to the outer environment by sacrificial dissolution of the coating layer. The higher absorption rate of hydrogen was more pronounced in corroded GI-coated steel caused by the comparatively larger cathodic polarization applied to the exposed substrate near the Zn layer, and a more severe form of coating dissolution (i.e., a broader area of the exposed substrate) by aqueous corrosion. In contrast, the corrosive species can only penetrate through the pre-existing cracks and pores in the Fe-Zn intermetallic phase (i.e., mostly, δ phase) of the GA coating, and the driving force for hydrogen evolution by H_2O reduction on GA-coated steel becomes smaller. The much broader corrosion damage in the GI coating layer forms a galvanic couple between the coating layer and exposed substrate, leading to a much larger quantity of absorbed and permeated hydrogen in the steel substrate. This increases the susceptibility to the hydrogen-assisted intergranular cracking with a quasi-cleavage pattern in a neutral corrosive environment.

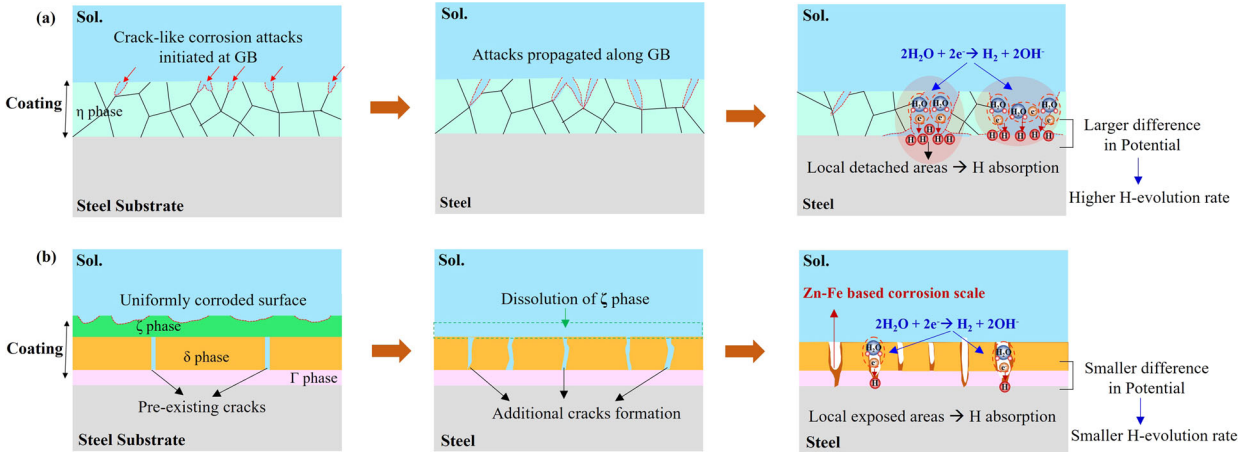

Fig. 14 Schematic diagrams of the corrosion and hydrogen penetration mechanisms. a, b GI and GA-coated steels, respectively.

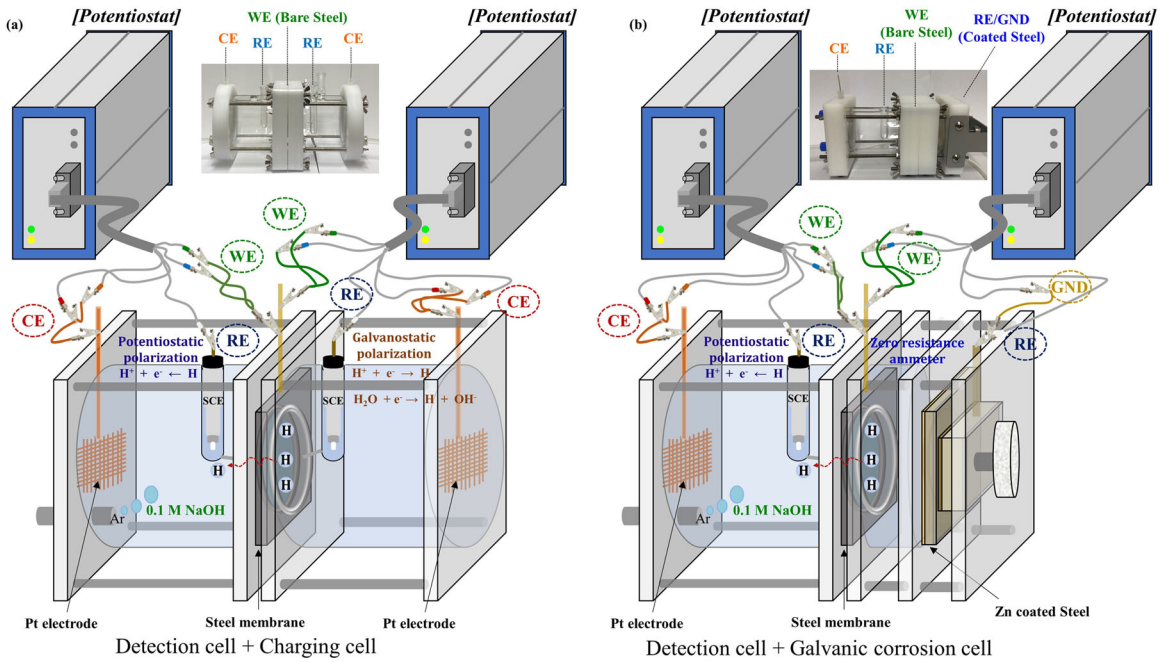

Fig. 15 Schematic diagram of the permeation apparatus. a Typical permeation apparatus (hydrogen charging cell + hydrogen detection cell). **b** Modified permeation apparatus (galvanic corrosion cell + hydrogen detection cell).

METHODS

Sample preparation and microstructural examination

To produce steel substrates, the steel samples were heated to 1150–1300 °C for 2 h, and hot and cold-rolled to a 1.2 mm thickness. The steel sheets were then austenitized at 780–840 °C for 200–400 s and cooled rapidly to ambient temperature. After mechanical polishing with a final polishing step of 0.04 μm, the microstructure of the steel sample was examined by field-emission scanning electron microscopy (FE-SEM), transmission electron microscopy (TEM), and electron back-scatter diffraction (EBSD) analysis with an acceleration voltage, beam current, and step size of 20 kV, 1 nA, and 40 nm, respectively. In addition, the fine precipitates were analyzed by TEM using an extraction replica sample.

The surface and cross-section morphologies of the GI and GA layers formed on the steel substrate were observed by FE-SEM. Prior to the cross-section observations, the samples were mounted with an epoxy resin and polished to 0.5 μm with an oil-based diamond suspension. The samples were then cleaned ultrasonically in ethanol and dried.

Electrochemical potentiodynamic polarization test and numerical curve-fitting

The electrochemical experiments were carried out using a conventional three-electrode cell consisting of a sample, a Pt grid, and a saturated calomel electrode (SCE), which served as a working, counter, and reference electrode, respectively. Before the experiments, the steel samples were ground to 2000 grit sand-paper, cleaned ultrasonically in ethanol, and dried. The coating samples were cleaned ultrasonically in ethanol and dried without pre-grinding. The potentiodynamic polarization test was conducted in a 3.5% NaCl + 0.3% NH_4SCN solution (pH: 6.78) at 25 °C. The potential was applied and scanned potentiodynamically at a scan rate of 0.2 mV s^{-1} from −500 mV to +250 mV vs. the open circuit potential. The polarization behaviors were analyzed by a numerical model based on the mixed potential theory under the assumptions that the current distribution is uniform over the sample surface, and the kinetic/transport parameters are uniform all over the system. From the theoretical model based on the mixed potential theory, several reaction parameters (i.e., exchange current density, Tafel constants, limiting current density, corrosion current density, and corrosion potential) were determined quantitatively by curve-fitting to

the polarization data. Moreover, under the conditions of galvanic couple formation, in which the steel substrate is exposed to the corrosive environment due to corrosion damage of the coating layers, the extents of cathodic overpotential and increased cathodic current density on steel were also obtained.

Electrochemical stripping experiment

An electrochemical stripping experiment for the two coated steel samples was carried out by applying a constant current density of 2 mA cm^{-2} in a 3.4 M NaCl + 0.3 M $ZnSO_4$ solution (pH: 4) at room temperature, and a potential transition curves with immersion time were obtained. The solution used was chosen in reference to a previous study[39].

Electrochemical permeation experiments

The hydrogen absorption and permeation behaviors were evaluated using an electrochemical permeation experiment, which were carried out using a Devanathan-Stachurski cell[40] designed in reference to ISO 17081[41]. Figure 15a illustrates a schematic diagram of the permeation apparatus, consisting of the two glass-type cells (charging and detection cells). The coated samples on one or both sides were removed by mechanical polishing. While polishing on one side of the sample, the other side was covered with lacquer to prevent corrosion. After polishing, lacquer was removed ultrasonically in acetone. An ~100 nm thin palladium layer was then deposited electrochemically on the side from which the coating has been removed. The electrodeposition conditions can be referred to previous study[42,43]. The permeation cell was assembled with the prepared sample. The detection side was filled with a deaerated 0.1 M NaOH solution, and a potential of +270 mV_{SCE} was applied and maintained during the permeation experiment. This potential allows the oxidation of the atomic hydrogen that diffused through the sample. Once the background current density reached a steady-state below 0.1 μA cm^{-2}, the charging cell was filled with a 3.5% NaCl + 0.3% NH_4SCN solution. The sample was then polarized galvanostatically with a cathodic current density of 1 mA cm^{-2} for constant hydrogen charging.

Because the permeation experiment under the applied cathodic current provides the ideal condition (i.e., a constant hydrogen influx by excluding the corrosion reaction in the charging side), the permeation experiment was also conducted without an external current input in the charging side. The coated sample surface was exposed naturally to the corrosive solution (i.e., a 3.5% NaCl). For the ease of measuring the permeation current, the small amount of NH_4SCN (0.3%) which can promote hydrogen absorption was also added in the solution.

Moreover, for a further mechanistic study on the hydrogen absorption and permeation behaviors of the coated steel sample, the charging side of the permeation apparatus was modified to measure the galvanic current flow between the coating layer and bare steel (i.e., both coating layers removed), which was designed in reference to the work reported by Kitahara et al.[44]. For this experiment, the bare steel was located in the center of the permeation cell, and the coating layer was connected to the counter electrode via a zero ammeter to measure the galvanic current density, i_{gal}, during the sacrificial dissolution of the coating layer. Figure 15b presents a brief sketch of the modified permeation apparatus. The other experimental conditions were the same as described above.

Surface and cross-section morphologies observation after the immersion test

An immersion test of the two coated steel samples was conducted in a 3.5% NaCl + 0.3% NH_4SCN solution for 168 h. The surface and cross-section morphologies were observed by FE-SEM at 3, 24, 72, and 168 h. For the cross-section observations, the corroded samples were mounted with an epoxy resin and polished to 0.5 μm with an oil-based diamond suspension. The samples were then cleaned ultrasonically in ethanol and kept in a vacuum desiccator until the FE-SEM observations.

Surface analysis using a three-dimensional surface profiler

Three-dimensional laser scanning with a confocal microscope (3D LSCM, VK-X1000, Keyence, Osaka, Japan) was conducted to analyze the surface characteristics of the two coating samples after immersion in a 3.5% NaCl + 0.3% NH_4SCN for 24, 72, and 168 h. Immediately after immersion, the samples were cleaned ultrasonically in ethanol and kept in a vacuum desiccator until surface analysis. The average surface roughness (R_a) for the two coating samples, which had been corroded for 168 h, was obtained from the surface analysis results.

Four-point bent beam test

The susceptibility of the two coated steel samples to hydrogen-assisted cracking was assessed using a four-point bent beam test in the same solution as the immersion test for 120 h, which was in reference to ASTM G39[45]. The applied stress in the bent beam test was kept at 100% of the yield strength (YS) of the steel sample. For the failed sample, the fracture surface was observed using FE-SEM.

DATA AVAILABILITY

The data that support the plots and other findings of the current study are available from the corresponding author upon reasonable request.

Received: 10 November 2021; Accepted: 12 March 2022;
Published online: 19 April 2022

REFERENCES

1. Lovicu, G. et al. Hydrogen embrittlement of automotive advanced high-strength steels. *Metall. Mater. Trans. A* **43**, 4075–4087 (2012).
2. Wint, N., Leung, J., Sullivan, J. H., Penny, D. J. & Gao, Y. The galvanic corrosion of welded ultra-high strength steels used for automotive application. *Corros. Sci.* **136**, 366–373 (2018).
3. Olsson, K. & Sperle, J. O. New advanced ultra-high strength steel for the automotive industry. *Auto. Technol.* **6**, 46–49 (2006).
4. Nie, Y. et al. Hydrogen embrittlement of a 1500-MPa tensile strength level steel with an ultrafine elongated grain structure. *Metall. Mater. Trans. A* **43**, 1670–1687 (2012).
5. Komazaki, S., Maruyama, R. & Misawa, T. Effect of applied cathodic potential on susceptibility to hydrogen embrittlement in high strength low alloy steel. *ISIJ Int.* **43**, 475–481 (2003).
6. Cho, L. et al. Influence of vanadium on the hydrogen embrittlement of aluminized ultra-high strength press hardening steel. *Mater. Sci. Eng. A* **735**, 448–455 (2018).
7. Park, J. S., Seong, H. G. & Kim, S. J. Effect of heat treatment conditions on corrosion and hydrogen diffusion behaviors of ultra-strong steel used for automotive applications. *Corros. Sci. Technol.* **18**, 267–276 (2019).
8. Fujimoto, N., Sawada, T., Tada, E. & Nishikata, A. Effect of pH on hydrogen absorption into steel in neutral and alkaline solution. *Mater. Trans.* **58**, 211–217 (2017).
9. Bockris, J. O. 'M. & Potter, E. C. The mechanism of the cathodic hydrogen evolution reaction. *J. Electrochem. Soc.* **99**, 169–186 (1952).
10. Nishimura, R., Shiraishi, D. & Maeda, Y. Hydrogen permeation and corrosion behavior of high strength steel MCM 430 in cyclic wet-dry SO_2 environment. *Corros. Sci.* **46**, 225–243 (2004).
11. Viana, P. R. P., Sousa, F. V. V. D., Barcia, O. E., Tribollet, B. & Mattos, O. R. Hydrogen reaction analysis in aqueous solutions containing H_2S/CO_2 at different pressures. *Corros. Sci.* **176**, 108938 (2020).
12. Wang, Z., Kan, B., Xu, J. & Li, J. The effect of second tempering on hydrogen embrittlement of ultra-high-strength steel. *Metall. Mater. Trans. A* **51**, 2811–2821 (2020).
13. Hojo, T., Kobayashi, J., Sugimoto, K., Nagasaka, A. & Akiyama, E. Effect of alloying elements addition on delayed fracture properties of ultra-high-strength trap-aided martensitic steels. *Metals* **10**, 6 (2020).
14. Choi, Y. I., Shin, E. S., Kuroda, K., Okido, M. & Park, C. J. Improved surface morphology and corrosion resistance for galvannealed coatings by pre-electroplating iron. *Corros. Sci.* **58**, 152–158 (2012).
15. Chakraborty, A. & Ray, R. K. Influence of microstructure and texture on the formability character of industrially produced galvannealed coatings on three interstitial free steels. *Surf. Coat. Technol.* **203**, 1756–1764 (2009).
16. Queiroz, F. M. & Costa, I. Electrochemical, chemical and morphological characterization of galvannealed steel coating. *Surf. Coat. Technol.* **201**, 7024–7035 (2007).
17. Liu, Y., Ooi, A., Tada, E. & Nishikata, A. Electrochemical monitoring of the degradation of galvanized steel in simulated marine atmosphere. *Corros. Sci.* **147**, 273–282 (2019).
18. Tahara, A. & Kodama, T. Potential distribution measurement in galvanic corrosion of Zn/Fe couple by means of Kelvin prove. *Corros. Sci.* **42**, 655–673 (2000).
19. Lee, J. K. Kinetics of hydrogen movement in Zn. *J. Korean Phys. Soc.* **51**, 1320–1324 (2007).

20. Sriraman, K. R., Brahimi, S., Szpunar, J. A. & Yue, S. Hydrogen embrittlement of Zn, Zn-Ni and Cd-coated high strength steel. *J. Appl. Electrochem.* **43**, 441–451 (2013).
21. Zakrocymski, T. Adaptation of the electrochemical permeation technique for studying entry, transport and trapping of hydrogen in metals. *Electrochim. Acta* **51**, 2261–2266 (2006).
22. Goodwin, F. E. Developments in the production of galvannealed steel for automotive. *Trans. Indian Inst. Met.* **66**, 671–676 (2013).
23. Lin, C. S., Meshii, M. & Cheng, C. C. Phase evolution in galvanneal coatings on steel sheets. *ISIJ Int.* **35**, 503–511 (1995).
24. Ha, H. Y., Park, S. J., Kang, J. Y., Kim, H. D. & Moon, M. B. Interpretation of the corrosion process of a galvannealed coating layer on dual-phase steel. *Corros. Sci.* **53**, 2430–2436 (2011).
25. Zhang, K., Li, Z., Wang, Z., Sun, X. & Yong, Q. Precipitation behavior and mechanical properties of hot-rolled high strength Ti–Mo-bearing ferritic sheet steel: The great potential of nanometer-sized (Ti, Mo)C carbide. *J. Mater. Res.* **31**, 1254–1263 (2016).
26. Nakagawa, Y., Tada, M., Kojima, K. & Nakamaru, H. Effect of Nb contents on size of ferrite grains and Nb precipitates in ultra-low carbon steel for cans. *ISIJ Int.* **56**, 1262–1267 (2016).
27. Chen, C. Y. et al. Precipitation hardening of high-strength low-alloy steels by nanometer-sized carbides. *Mater. Sci. Eng. A* **499**, 162–166 (2009).
28. Chen, L. et al. Corrosion behaviors of Q345R steel at the initial stage in an oxygen-containing aqueous environment: experiment and modeling. *Materials* **11**, 1462 (2018).
29. Jones, D. A. *Principles and Prevention of Corrosion* (Prentice Hall, 1996).
30. Park, J. S., Lee, H. J. & Kim, S. J. Electrochemical corrosion and hydrogen diffusion behaviors of Zn and Al coated hot-press forming steel sheets in chloride containing environments. *Korean J. Mater. Res.* **28**, 286–294 (2018).
31. Cao, J. L., Li, L. T., Wu, J. X., Lu, Y. P. & Gui, Z. L. Diffusion of hydrogen in a steel substrate absorbed during zinc and zinc-silica electroplating. *Corrosion* **58**, 698–702 (2002).
32. Han, K., Lee, I., Ohnuma, I., Okuda, K. & Kainuma, R. Micro-Vickers hardness of intermetallic compounds in the Zn-rich portion of Zn–Fe binary system. *ISIJ Int.* **58**, 1578–1583 (2018).
33. Evers, S., Senöz, C. & Rohwerder, M. Spatially resolved high sensitive measurement of hydrogen permeation by scanning Kelvin probe microscopy. *Electrochim. Acta* **110**, 534–538 (2013).
34. Ogle, K., Morel, S. & Jacquet, D. Observation of self-healing functions on the cut edge of galvanized steel using SVET and pH microscopy. *J. Electrochem. Soc.* **153**, B1–B5 (2006).
35. Krieg, R., Rohwerder, M., Evers, S., Schuhmacher, B. & Schauer-Pass, J. Cathodic self-healing at cut-edges: the effect of Zn^{2+} and Mg^{2+} ions. *Corros. Sci.* **65**, 119–127 (2012).
36. Abadias, G. et al. Review article: stress in thin films and coatings: current status, challenges, and prospects. *J. Vac. Sci. Technol. A* **36**, 020801 (2018).
37. Kim, S. J. Effect of the elastic tensile load on the electrochemical corrosion behavior and diffusible hydrogen content of ferritic steel in acidic environment. *Int. J. Hydrog. Energy* **42**, 19367–19375 (2017).
38. Yang, W. J., Yang, P., Li, X. M. & Feng, W. L. Influence of tensile stress on corrosion behavior of high-strength galvanized steel bridge wires in simulated acid rain. *Mater. Corros.* **63**, 401–407 (2012).
39. Besseyrias, A., Dalard, F., Rameau, J. J. & Baudin, H. Electrochemical behavior of zinc-iron intermetallic compounds in an aqueous solution containing NaCl and $ZnSO_4$. *Corros. Sci.* **39**, 1883–1896 (1997).
40. Devanathan, M. A. V. & Stachurski, Z. The adsorption and diffusion of electrolytic hydrogen in palladium. *Proc. R. Soc. Lond. A* **270**, 90–102 (1962).
41. British Standard European Norm. *ISO 17081. Method of Measurement of Hydrogen Permeation and Determination of Hydrogen Uptake and Transport in Metals by an Electrochemical Technique* (BS EN Standards, 2014).
42. Kim, S. J., Yun, D. W., Jung, H. G. & Kim, K. Y. Determination of hydrogen diffusion parameters of ferritic steel from electrochemical permeation measurement under tensile loads. *J. Electrochem. Soc.* **161**, 173–181 (2014).
43. Kim, S. J. et al. A mechanistic study on the hydrogen trapping property and the subsequent electrochemical corrosion behavior of quenched and tempered steel. *Int. J. Hydrog. Energy* **43**, 17912–17920 (2018).
44. Kitahara, G., Tsuji, A., Asada, T. & Suzuki, T. Assessment of hydrogen absorption and delayed fracture limit of high tensile steel sheet in corrosive environment. *RD Rev. Toyota CRDL* **50**, 23–31 (2019).
45. ASTM G39. *Standard Practice for Preparation and Use of Bent-Beam Stress-Corrosion Test Specimens* (ASTM International, 2016).

ACKNOWLEDGEMENTS

This research was supported in part by the National Research Foundation of Korea (NRF) grant funded by the Korea government (MSIT) (Nos. 2019R1C1C1005007, 2022R1A2C4001255).

AUTHOR CONTRIBUTIONS

S.J.K.: writing—original draft, writing—review and editing, methodology, project administration, funding acquisition. J.S.P.: investigation, visualization, writing—review and editing. S.P.J.: project administration, conceptualization.

COMPETING INTERESTS

The authors declare no competing interests.

ADDITIONAL INFORMATION

Supplementary information The online version contains supplementary material available at https://doi.org/10.1038/s41529-022-00245-1.

Correspondence and requests for materials should be addressed to Sung Jin Kim.

Reprints and permission information is available at http://www.nature.com/reprints

Publisher's note Springer Nature remains neutral with regard to jurisdictional claims in published maps and institutional affiliations.